Iranian Journal of Basic Medical Sciences

ijbms.mums.ac.ir

IJBMS

A bilayer strategy for wound healing: *In vitro* assessment of alginate-PVA-BG hydrogel and AgNPs-loaded chitosan scaffolds

Elham Rahmanian Koshkaki [1, 2], Farzaneh Dehghani [1, 3]*, Hossein Bordbar [1, 3], Nader Tanideh [4, 5], Zahra Zareshahrabadi [6], Ali Mohammad Amani [7], Salar Khajehpour [8], Ahmad Vaez [3, 8, 9]*

[1] Department of Anatomy, Faculty of Medicine, Shiraz University of Medical Sciences, Shiraz, Iran
[2] Student Research Committee, Shiraz University of Medical Sciences, Shiraz, Iran
[3] Histomorphometry and Stereology Research Center, Shiraz University of Medical Sciences, Shiraz, Iran
[4] Stem Cells Technology Research Center, Shiraz University of Medical Sciences, Shiraz, Iran
[5] Department of Pharmacology, Medical School, Shiraz University of Medical Sciences, Shiraz, Iran
[6] Basic Sciences in Infectious Diseases Research Center, Shiraz University of Medical Sciences, Shiraz, Iran
[7] Department of Medical Nanotechnology, School of Advanced Medical Sciences and Technologies, Shiraz University of Medical Sciences, Shiraz, Iran
[8] Department of Tissue Engineering and Applied Cell Sciences, School of Advanced Medical Sciences and Technologies, Shiraz University of Medical Sciences, Shiraz, Iran
[9] Biotechnology Research Center, Shiraz University of Medical Sciences, Shiraz, Iran

ARTICLE INFO

Article type:
Original

Article history:
Received: Mar 11, 2026
Accepted: Jul 21, 2026

Keywords:
Bioglass
Hydrogel
Nanoparticles
Scaffold
Wound healing

ABSTRACT

Objective(s): Developing multifunctional wound dressings requires integrating antimicrobial barriers with regenerative hydrogel matrices. This study engineered a bilayer scaffold comprising an upper electrospun chitosan (Cs)-polyethylene oxide (PEO) layer loaded with green-synthesized silver nanoparticles (AgNPs) and a lower lyophilized alginate (Alg)-polyvinyl alcohol (PVA) hydrogel layer enriched with bioactive glass (BG).

Materials and Methods: AgNPs were synthesized using plant-derived proteolytic enzymes and characterized by DLS and UV-Vis spectroscopy. The electrospun upper layer was fabricated via electrospinning, while the lower hydrogel layer was prepared by freeze-drying. The Alg-PVA-BG hydrogel network was characterized for swelling behavior (gravimetrically at 37 ˚C), degradation kinetics, porosity, and mechanical integrity. Biological evaluations included an MTT cytocompatibility assay using L929 murine fibroblasts over 1, 3, and 5 days, a wound closure assay using HaCaT human keratinocytes over 48 hr, and antibacterial activity against *Staphylococcus aureus* and *Escherichia coli* using MIC90 determination.

Results: BG incorporation (20% w/w) modulated the hydrogel structure, resulting in optimized porosity (58-67%), controlled swelling ratios (147.5-189.0%), and enhanced mechanical stability. The AgNP-loaded top layer (32 µg/ml) exhibited potent broad-spectrum antibacterial activity with MIC90 values of 8.2 µg/ml against *S. aureus* and 12.5 µg/ml against *E. coli*. *In vitro* biological evaluations demonstrated excellent cytocompatibility (cell viability >85% for all groups) and significantly enhanced HaCaT cell migration (42.64±5.84%) for the Cs-PEO-AgNPs/Alg-PVA-BG group compared to the control group ($P<0.05$)..

Conclusion: These results demonstrate the synergistic efficacy of combining an AgNP-mediated antimicrobial barrier with a bioactive alginate-based hydrogel matrix, offering a robust strategy for advanced wound-healing applications.

▶ Please cite this article as:
Rahmanian Koshkaki E, Dehghani F, Bordbar H, Tanideh N, Zareshahrabadi Z, Amani AM, Khajehpour S, Vaez A. A bilayer strategy for wound healing: *In vitro* assessment of alginate-PVA-BG hydrogel and AgNPs-loaded chitosan scaffolds. Iran J Basic Med Sci 2026; 29: 1835-1845. doi: https://dx.doi.org/10.22038/ijbms.2026.94976.20487

Introduction

The skin serves as a critical barrier against environmental threats, and disruption in full-thickness wounds significantly delays healing and increases the risk of infection (1, 2). Effective management remains a clinical challenge, necessitating advanced strategies beyond traditional dressings (3). Tissue engineering offers a viable solution by developing bioactive scaffolds that mimic the extracellular matrix (ECM) and deliver pharmacological cues to modulate cellular behavior (4, 5).

Chitosan (Cs), a naturally occurring polysaccharide derived from chitin, exhibits inherent biocompatibility, biodegradability, and antibacterial properties due to its cationic nature, which interacts with negatively charged bacterial membranes. However, Cs suffers from low spinnability, limiting its application in electrospinning. Blending Cs with polyethylene oxide (PEO), a synthetic biocompatible polymer, enhances processability and fiber

**Corresponding authors:* Ahmad Vaez. Department of Tissue Engineering and Applied Cell Sciences, School of Advanced Medical Sciences and Technologies, Shiraz University of Medical Sciences, Shiraz, Iran. Email: ahmadvaez@sums.ac.ir; Farzaneh Dehghani. Department of Anatomy, Faculty of Medicine, Shiraz University of Medical Sciences, Shiraz, Iran. Email: dehghanf@sums.ac.ir

© 2026. This work is openly licensed via CC BY 4.0.
This is an Open Access article distributed under the terms of the Creative Commons Attribution License (https://creativecommons.org/licenses), which permits unrestricted use, distribution, and reproduction in any medium, provided the original work is properly cited.

uniformity while maintaining biocompatibility (6). Previous studies have demonstrated that Cs-PEO electrospun scaffolds support cell adhesion and proliferation, making them suitable for wound dressing applications (7, 8).

To further enhance antimicrobial efficacy, silver nanoparticles (AgNPs) have been widely incorporated into wound dressings due to their broad-spectrum activity against both Gram-positive and Gram-negative bacteria (9). Green synthesis of AgNPs using plant extracts or enzymes has gained attention as an eco-friendly alternative to chemical methods, producing stable and biocompatible nanoparticles (10). Studies have reported that AgNPs exert antibacterial effects through the release of Ag^+ ions, which disrupt bacterial cell walls and interfere with intracellular processes (11, 12). However, the concentration of AgNPs must be carefully optimized to avoid cytotoxicity, as high doses can impair mammalian cell viability (13).

Conversely, the underlying regenerative layer requires moisture retention and bioactive signaling. Alginate (Alg), a natural anionic polysaccharide derived from brown algae, is widely used in wound dressings for its excellent biocompatibility, high water absorption capacity, and gel-forming ability in the presence of divalent cations such as Ca^{2+} (14). However, pure alginate hydrogels often lack sufficient mechanical strength for long-term wound coverage (15). Combining Alg with polyvinyl alcohol (PVA), a synthetic polymer with good mechanical properties and biocompatibility, has been shown to improve hydrogel structural integrity and stability while maintaining a moist healing environment (16, 17). Several studies have reported that Alg-PVA blends provide controlled swelling, adequate porosity, and suitable degradation rates for wound-healing applications (10, 18).

Functionalization with bioactive glass (BG) further enhances this matrix by releasing therapeutic ions (e.g., Ca^{2+}, Si^{4+}) that stimulate cellular migration, proliferation, and tissue regeneration (19, 20). BG particles have been extensively studied for their ability to form a hydroxyapatite (HA) layer upon immersion in physiological fluids, which promotes osteoconductivity and soft tissue integration (12). Additionally, ionic dissolution products from BG have been shown to up-regulate the expression of vascular endothelial growth factor (VEGF) and other growth factors involved in angiogenesis and wound healing (21). Previous investigations have established the bioactivity of BG compositions such as 45S5 and S53P4, leading to their clinical application in soft tissue repair (22). More recent reports have demonstrated that BG incorporation into polymeric hydrogels enhances fibroblast migration and collagen deposition, highlighting their potential for skin regeneration (12). However, controlled release of these ions is crucial to prevent adverse effects such as excessive inflammation or calcification (23).

Hydrogel-based systems are particularly promising due to their high-water content and porous structure, facilitating gas exchange and exudate absorption (10, 12). Furthermore, hydrogel networks can be engineered to encapsulate and sustain the release of bioactive ions, ensuring prolonged activity at the wound site (24). Crucially, their soft, hydrated structure closely mimics the native ECM, providing structural support that promotes cellular infiltration and tissue regeneration (18).

Despite the individual advantages of these components, few studies have systematically combined an antimicrobial electrospun layer with a bioactive hydrogel layer in a bilayer construct for wound healing applications. This study addresses this gap by engineering a biomimetic bilayer scaffold comprising an upper AgNPs-loaded Cs-PEO electrospun layer and a lower BG-enriched Alg-PVA hydrogel. We comprehensively characterized the physicochemical properties of the dual-layered scaffold and evaluated its *in vitro* biological performance. Our findings demonstrate the synergistic potential of this bilayer design for advanced wound healing applications.

Materials and Methods

Materials and reagents

All materials and reagents were procured from the following sources: Chitosan (Cs, medium molecular weight, 80% degree of deacetylation, Iran Chitosan), Polyethylene oxide (PEO, Mv~1,000,000), Alginate (Alg), Polyvinyl alcohol (PVA), Sodium nitrate ($NaNO_3$), calcium nitrate tetrahydrate ($Ca(NO_3)_2{\cdot}4H_2O$), Calcium chloride ($CaCl_2$), and glutaraldehyde from Sigma; tetraethyl orthosilicate (TEOS), triethyl phosphate (TEP), nitric acid, and silver nitrate ($AgNO_3$) from Merck; Dulbecco's Modified Eagle Medium (DMEM) and fetal bovine serum (FBS) from Gibco; and MTT assay kit and phosphate-buffered saline (PBS) from DNAbiotech. The Shiraz Center for Comparative and Experimental Medicine provided the L929 murine fibroblast cell line.

Green synthesis of AgNPs

In alignment with eco-friendly nanotechnology principles, AgNPs were synthesized using a green reduction method with Bromelain solution. To prepare the bromelain extract, 10 g of bromelain powder was dissolved in 100 ml of deionized water and heated at 80 ˚C for 2 hrs with stirring. Subsequently, a 1 mM $AgNO_3$ solution was added to the extract and stirred for 6 h to allow nanoparticle formation. The resulting dark brown solution was centrifuged at 10,000 rpm for 20 minutes to purify the AgNPs. The pellets were washed with deionized water to remove unreacted ions, vacuum-dried at 80 ˚C for two days, and stored in a cool, dark place (12).

Fabrication of electrospun scaffolds

A 3% (w/v) Cs solution (0.125 g in 3 ml of 0.5 M acetic acid) and a PEO solution (0.031 g in 2 ml of 0.5 M acetic acid) were prepared separately. The two were mixed at a 4:1 ratio (Cs:PEO) to form a uniform polymer blend, into which AgNPs were incorporated at an optimized concentration of 32 µg/ml based on preliminary antibacterial assays. Electrospinning was performed at 18 kV with a 160 mm tip-to-collector distance and a flow rate of 0.5 ml/h (Nanofanavaran, Iran). The collector operated at 150 rpm rotational speed and 1.5 mm/s linear speed. The resulting nanofibrous mats were cross-linked by exposure to 25% glutaraldehyde vapor for 48 hours, followed by three 20-minute washes with distilled water to remove residual glutaraldehyde (10).

Synthesis of BGs

According to earlier reports, 45S5 BG was synthesized using the sol-gel process (12). TEOS (13.7 ml) and TEP (1.37 ml) were added to a nitric acid solution and stirred

for 30 min. Subsequently, 7.75 g of $Ca(NO_3)_2 \cdot 4H_2O$ and 4.85 g of $NaNO_3$ were added separately and stirred until completely dissolved. The sol was left undisturbed at 25 ˚C for 24 hours to induce gelation. The resulting gel was then dried in an oven at 70 ˚C for 24 hours. After thermal stabilization at 200 ˚C for five hours in an electric furnace, the dried material was calcined at 700 ˚C for two hours with a controlled heating rate of 10 ˚C/min. The final product was ground into a fine powder using ball milling.

Synthesis of Alg-PVA hydrogels

A homogeneous Alg-PVA blend was prepared by mixing 2% (w/v) alginate and 10% (w/v) PVA solutions in a 1:1 volumetric ratio under continuous stirring. BG particles were then incorporated at concentrations of 5%, 10%, 20%, and 40%(w/w relative to the polymer) and homogenized for 1 hour to ensure uniform dispersion. Gelation was initiated by the dropwise addition of a 1%(w/w) $CaCl_2$ solution, inducing ionic cross-linking of alginate chains via Ca^{2+} ions to form an 'egg-box' structure. At the same time, PVA contributed to mechanical reinforcement through hydrogen bonding within the polymer network. The resulting suspensions were cast into cylindrical Teflon molds (2 cm diameter × 1 cm height), frozen at -80 ˚C for 24 hours, and subsequently lyophilized at -54 ˚C under vacuum for 24 hours using a Telstar freeze-dryer(Terrassa, Spain)(10).

Physicochemical characterization of particles

Morphology and size analysis

The structural and dimensional characteristics of AgNPs were assessed using scanning electron microscopy (SEM; VEGA3 TESCAN). The hydrodynamic size distribution and polydispersity of the generated AgNPs were measured using dynamic light scattering (DLS) at 25 ˚C.

Fourier transform infrared (FTIR) spectroscopy and X-ray diffraction (XRD) analysis

A Thermo Nicolet NEXUS 670 spectrometer was used to record the FTIR spectra. Before analysis, the samples were processed into KBr pellets. With a scan rate of 120 scans/min and a resolution of 4 cm^{-1}, all spectra were gathered within the wavenumber range of 500 to 4500 cm^{-1} (25). XRD analysis was performed using a Bruker Advance D8 diffractometer to assess the crystal structure and phase composition of the materials (25).

HA formation

We compressed pellets of BGs (1 g), sintered them at 300 ˚C, and submerged them in 15 mL of PBS for seven days to investigate bioactivity. We then used SEM to examine the development of hydroxyapatite (HA) on the pellet surfaces (12, 26).

Physicochemical characterization of scaffolds

Degradation study

Lyophilized Alg-PVA and Alg-PVA-BGs hydrogels, along with Cs-PEO and Cs-PEO-AgNPs samples, were evaluated to assess the degradation behavior. Cs-PEO-AgNPs electrospun nanofibrous mats and these lyophilized hydrogels were submerged in PBS at 37 °C (10). To determine the rate of deterioration, mass loss was evaluated for the scaffolds after 7, 14, and 21 days and for the hydrogels after 1, 3, and 5 days. Equation (Eq.1) was used to determine the degradation rate:

$$\text{Weight loss (\%)}=(W_0-W_1)/W_0 \times 100 \quad (1)$$

Where W_0 and W_1 are the initial weight and dry weight of subjects after being removed from PBS, respectively.

Swelling test

Alg-PVA and Alg-PVA-BGs hydrogels, along with Cs-PEO and Cs-PEO-AgNPs samples, were submerged in PBS (pH 7.4) and kept at 37 ˚C for 24 hours to examine the swelling behavior of the lyophilized hydrogels and electrospun scaffolds (27).

Contact angle evaluation

A static contact angle analyzer (SHARIF Solar CA500A, Iran) was used to measure the samples' water contact angle using the sessile drop technique to evaluate their wettability. Each sample surface received a 10 µl droplet of deionized water, and after three seconds, the contact angle was measured (18).

Porosity assessment

The usual ethanol displacement method was used to assess the porosity of the electrospun scaffolds and lyophilized hydrogels (10, 18). A predetermined volume of ethanol (V1) was put into a graduated cylinder. To fill all the pores and eliminate air bubbles, samples of known weight were added to the ethanol and gently stirred. V2 was the new total volume that was noted. The volume of the residual ethanol was measured as V3 after the sample was removed. The following formula was then used to determine the porosity (Eq.2):

$$\text{Porosity (\%)} =(V_1-V_3)/(V_2- V_3)\times 100 \quad (2)$$

Water vapor transmission rate (WVTR) study

In accordance with the applicable ASTM standard, the WVTR of the electrospun scaffolds was assessed to determine moisture permeability (28). Vials with a 1.35 cm2 opening diameter were filled with distilled water, and disc-shaped samples were fixed to them. The vials were then incubated at 37 ˚C and 50% relative humidity. Over 24 hours, the water weight (g) loss (ΔW) was recorded, and WVTR was computed using (Eq.3):

$$WVTR=\Delta W/A \quad (3)$$

Mechanical characterization

ASTM D882-02 was used to assess the tensile properties of Cs-PEO and Cs-PEO-AgNPs electrospun scaffolds. Rectangular specimens measuring 20×5×0.27 mm were subjected to uniaxial tensile testing on a universal testing machine at a crosshead speed of 1 mm/min. The resulting stress-strain curves were used to compute the mechanical parameters (18). These metrics included yield strength (determined using the 0.2% offset method), ultimate tensile strength (UTS, the maximum applied stress), elongation at break, and elastic modulus (estimated from the slope of the initial linear elastic region). Each group was tested on at least five specimens, and the results were reported as mean values.

Biological characterization

Antimicrobial analyses

Using the broth microdilution method, the Minimum

Inhibitory Concentration (MIC) and Minimum Microbicidal Concentration (MMC) of AgNPs were assessed against standard strains of *Escherichia coli* (ATCC 25922), *Pseudomonas aeruginosa* (ATCC 27853), *Enterococcus faecalis* (ATCC 11700), and *Staphylococcus aureus* (ATCC 52268). The bacterial inocula were introduced into Mueller-Hinton broth containing serial dilutions of AgNPs ranging from 1 to 256 µg/ml after being adjusted to the 0.5 McFarland standard. The MIC was determined as the lowest concentration that did not exhibit any discernible turbidity after 24 hours of incubation at 37 ˚C. Subculturing was used to determine the MMC, which was defined as the lowest dose that produced bacterial killing of at least 99.9% (n=3). Every experiment had suitable growth and sterility controls (29).

To evaluate the barrier functionality of the dressings, a microbial penetration assay was conducted. The samples were positioned over glass vials containing 5 ml of brain-heart infusion (BHI) broth, covering a defined test surface area of 0.8 cm^2. An open vial served as the positive control, while a vial sealed with a cotton ball was used as the negative control. Following incubation at ambient temperature for 3 and 7 days, the extent of microbial contamination was determined by measuring the optical density of the culture medium at 600 nm using a microplate spectrophotometer, with all tests performed in triplicate (n=3)(18).

Hemocompatibility evaluation

The hemolysis assay was carried out in accordance with a previously published procedure (30). Erythrocytes were separated from anticoagulated fresh whole blood by centrifuging it at 116 ×g for 10 minutes at 25 ˚C. The erythrocytes were then rinsed three times with PBS. After being cleaned, the erythrocytes were placed in a 24-well plate with the electrospun scaffolds and lyophilized hydrogels (Alg-PVA, Alg-PVA-BGs, Cs-PEO, and Cs-PEO-AgNPs) and incubated for two hours at 37 ˚C. Following incubation, the supernatant from each well was collected and centrifuged for 15 minutes at 115 ×g. A microplate reader was used to measure the samples' absorbance (s) at 550 nm. Using PBS as the negative control (n) and distilled water as the positive control (p), the hemolysis ratio was computed (Eq.4).

$$\text{Hemolysis (\%)}=(OD_s-OD_n)/(OD_p-OD_n)\times 100 \quad (4)$$

Cytocompatibility assessment

The cytocompatibility of the electrospun scaffolds (Cs-PEO and Cs-PEO-AgNPs) and lyophilized hydrogels (Alg-PVA and Alg-PVA-BGs) was assessed using the MTT assay at 1, 3, and 5 days. Before cell seeding, all samples were prepared using a sterile biopsy punch (6 mm diameter) and sterilized under UV light for 30 minutes on each side. The samples were then placed at the bottom of 96-well tissue culture plates. L929 murine fibroblasts were seeded directly onto the surface of each sample at a density of 10,000 cells per well in DMEM supplemented with 10% FBS (direct contact method). The negative control consisted of cells grown on tissue culture-treated plates without scaffolds. At each time point, the medium was removed, and the samples were gently washed with PBS. Then, 100 µl of MTT solution (0.5 mg/ml in DMEM) was added to each well and incubated for 4 hours at 37 ˚C. The resulting formazan crystals were dissolved in 100 µl of DMSO, and the optical density (OD) was measured at 570 nm using a BioTek ELx800 microplate reader. All experiments were performed in independent replicates (n=8)(31). Cell viability was calculated using the following formula (Eq.5):

$$\text{Cell viability (\%)}=(\text{OD of the samples})/(\text{OD of control})\times 100 \quad (5)$$

Migration assay

To evaluate cell migration, the scaffolds and lyophilized hydrogels were subjected to an indirect exposure method using sample extracts. The scaffolds and hydrogels were immersed in serum-free DMEM at ratios of 3 cm^3/ml and 0.5 cm^2/ml, respectively (surface area to liquid volume). DMEM alone served as the control. All test tubes were incubated on a shaker at 37 ˚C for two weeks. After incubation, the extracts were filtered through a 0.22 µm filter and then supplemented with 5% FBS and antibiotics before use (10, 12). HaCaT human keratinocytes were cultured in 24-well plates until they reached approximately 80% confluency. A sterile 200 µl pipette tip was used to create a uniform scratch across the monolayer. After washing with PBS to remove detached cells, the cells were treated with the prepared extracts and incubated for 48 hours at 37 ˚C with 5% CO_2. Images were captured at 0 and 48 hours, and wound closure percentage was calculated using the following formula (Eq.6):

$$\text{Wound closure (\%)}=1-(A_t)/A_0\times 100 \quad (6)$$

Statistical analysis

Statistical analyses were performed using GraphPad Prism software (version 6, USA). All data are expressed as mean±SD. To determine statistical significance, one-way ANOVA followed by Tukey's *post-hoc* test was performed. Significance levels were set at $P<0.05$.

Results

Physicochemical tests

AgNPs

The produced AgNPs had an average particle size of 293.22±2.27 nm and a mostly spherical shape, according to SEM analysis (Figure 1A). These results were further supported by DLS analysis, which showed a hydrodynamic size distribution in the 200-300 nm range (Figure 1B). The FTIR spectra of Bro-AgNPs exhibited characteristic bands associated with Ag-O bonding vibrations and metallic silver (31), along with signatures from organic functional groups including C-O deformation (32), C-H (bending and alkane stretching) (31), and C-N stretching and bending vibrations (33), as well as peaks attributed to carbonyl stretches (C=O), amide linkages (C=C), and absorptions indicative of O–H or N–H stretching (Figure 1C)(31). Also, the crystal structure and phase purity of the Ag NPs were confirmed by XRD analysis (Figure 1D), which showed characteristic metallic silver peaks at 2θ values of 38.13˚ (111), 44.32˚ (200), 64.48˚ (220), and 77.44˚ (311), matching the standard reference (JCPDS card No. 96-901-6253).

Electrospun scaffolds

At magnifications of 20 µm and 5 µm, SEM micrographs showed that the Cs-PEO scaffold had a homogeneous, bead-free fibrous structure with an average fiber diameter of

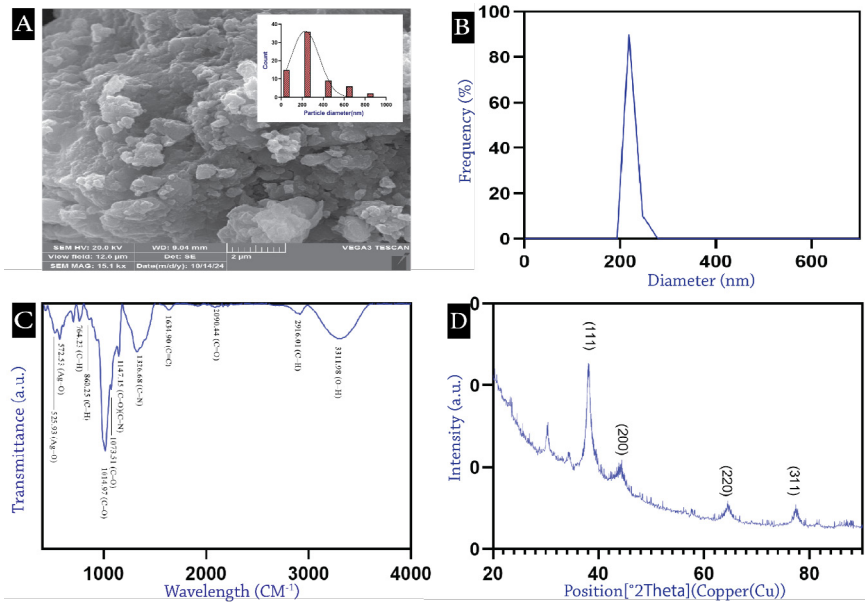

Figure 1. Physicochemical characterization of green-synthesized silver nanoparticles (AgNPs)
SEM micrograph showing spherical morphology and particle size distribution (A); DLS analysis confirming hydrodynamic size in the 200–300 nm range (B); FTIR spectra indicating Ag–O bonding and organic capping agents (C); XRD pattern verifying crystalline metallic silver phase (JCPDS No. 96-901-6253) (D)

0.76±0.33 µm (Figure 2A, B). Despite having a continuous fibrous architecture, the Cs-PEO-AgNPs scaffold showed a discernible decrease in fiber diameter, with an average of 0.40±0.23 µm (Figure 2C, D). Near-contact angle values for Cs-PEO scaffolds (61.12±5.87°) and Cs-PEO-AgNPs scaffolds (63.92±5.64°) were found by a surface wettability study (Figure 2E). The swelling ratios for Cs-PEO and Cs-PEO-AgNPs were 245.1±23.63% and 239.4±12.02%, respectively, after 24 hours (Figure 2F). At days 7, 14, and 21, the Cs-PEO scaffold showed degradation percentages of 29.41±2.38%, 54.96±5.40%, and 68.82±3.92%, respectively. Accordingly, degradation values for the Cs-PEO-AgNPs scaffold were 30.50±3.36%, 58.95±6.57%, and 71.19±7.17%, respectively (Figure 2G). The Cs-PEO and Cs-PEO-AgNPs scaffolds were found to have porosities of 66.16±3.44% and 71.31±4.04%, respectively. Accordingly, Cs-PEO's WVTR was 1227±119 g/m²/day, Cs-PEO-AgNPs' was 1250±237 g/m²/day, whereas the open container was 16805±4868 g/m²/day. For both scaffold types, weight loss increased gradually over time, according to the biodegradation study. The Cs-PEO-AgNPs scaffold had a higher Yield strength than Cs-PEO. The mechanical property results are reported in Figure 2H and Table 1.

Table 1. Mechanical properties of Cs-PEO and Cs-PEO-AgNPs scaffolds

Scaffolds	Yield strength	Elongation	UTS	Elastic module
Cs-PEO	2.80±0.61	10.73±1.10	5.93±0.61	1.71±0.13
Cs-PEO-AgNPs	4.55±0.63	12.07±1.22	6.57±0.86	1.74±0.08

The yield strength, UTS, and elastic modulus are reported in megapascals (MPa), while elongation is given as a percentage (%). ¨$P<0.01$
Cs-PEO: Chitosan polyethylene oxide; AgNPs: Silver nanoparticles

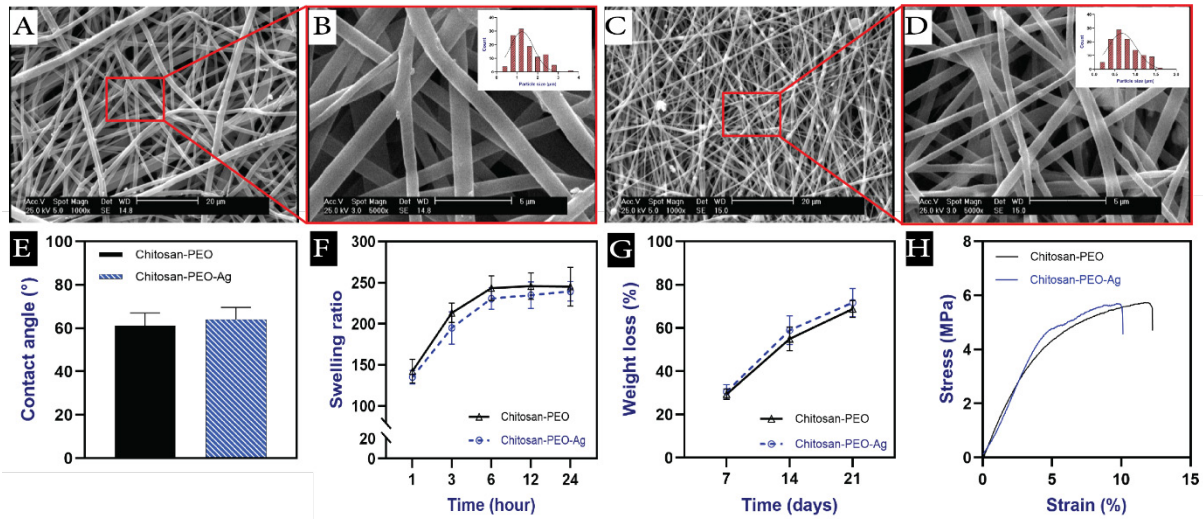

Figure 2. Characterization of chitosan polyethylene oxide (Cs-PEO) electrospun scaffolds
SEM images revealing bead-free fibrous architecture of Cs-PEO (A, B) and reduced fiber diameter upon AgNPs incorporation (C, D); surface wettability (E), swelling behavior (F), degradation profile (G), and tensile properties (H) demonstrating that AgNPs enhance mechanical strength while maintaining favorable hydrophilicity and biodegradability

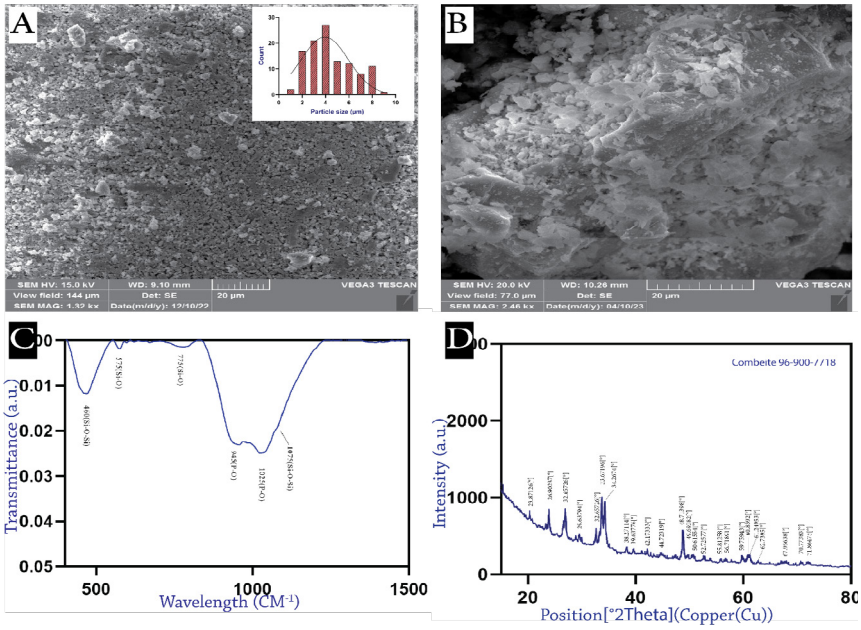

Figure 3. Bioactive glass (BG) characterization
SEM micrograph showing particle morphology and size (A); *in vitro* bioactivity evidenced by hydroxyapatite (HA) layer formation after PBS immersion (B); FTIR spectrum confirming silicate/phosphate network integrity (C); XRD pattern identifying crystalline phases of buchwaldite and cristobalite (D)

BG

The BG had an average particle size of 4.05±1.04 µm, according to SEM examination (Figure 3A). A HA layer was evidently formed on the BG surface following immersion in PBS at a liquid-to-solid ratio of 15:1 (v/w), showing *in vitro* bioactivity (Figure 3B). The functional groups of the glass network were represented by distinctive absorption bands in the FTIR spectrum of BG at 460, 575, 775, 945, 1025, and 1380 cm^{-1} (Figure 3C). The crystalline phases found in the BG were determined by XRD examination to be buchwaldite ($Na_{12}Ca_{12}P_{12}O_{48}$; JCPDS No. 96-901-1348) and cristobalite (Si_4O_8; JCPDS No. 96-900-9688)(Figure 3D).

Lyophilized hydrogels

The Alg-PVA lyophilized hydrogel showed an interconnected porous architecture with an average pore diameter of 16.12±3.01 µm, according to SEM examination (Figure 4A). When BG was added, the size of the pores decreased; the Alg-PVA-BG hydrogel's average pore width was 14.04±5.29 µm (Figure 4B). This reduction suggests that BG particles increased the cross-linking density within the polymer network. The incorporation of BG particles into the Alg-PVA matrix likely increased the cross-linking density through ionic interactions between Ca^{2+} (from BG) and carboxylate groups of alginates, resulting in reduced

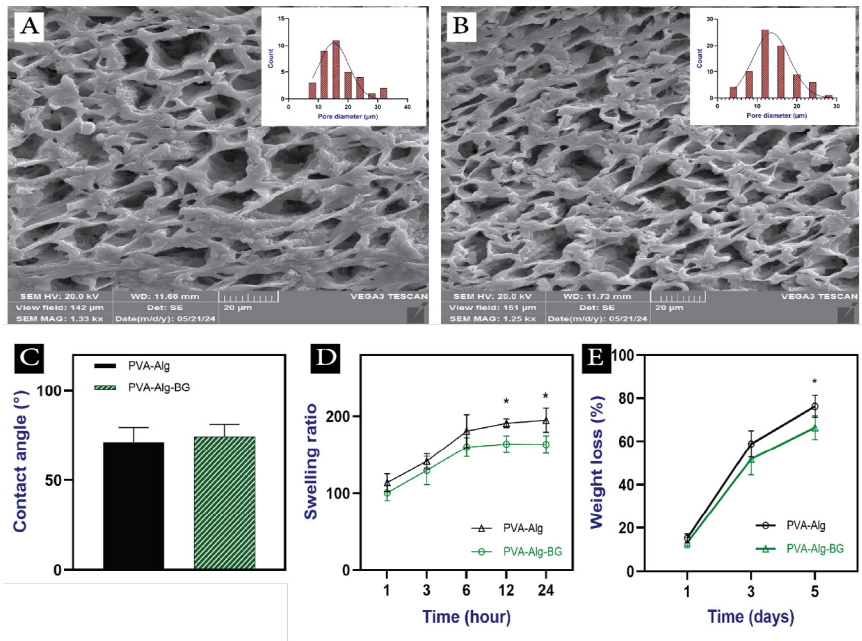

Figure 4. Microstructural and physicochemical characterization of alginate-polyvinyl alcohol (Alg-PVA) lyophilized hydrogels
SEM images reveal interconnected porous architecture in Alg-PVA (A) and reduced pore size upon BG incorporation (B). Surface wettability (C), swelling behavior (D), and degradation profiles (E) demonstrate that BG reinforcement modulates hydrogel network properties, enhancing stability while maintaining adequate hydration for wound healing applications

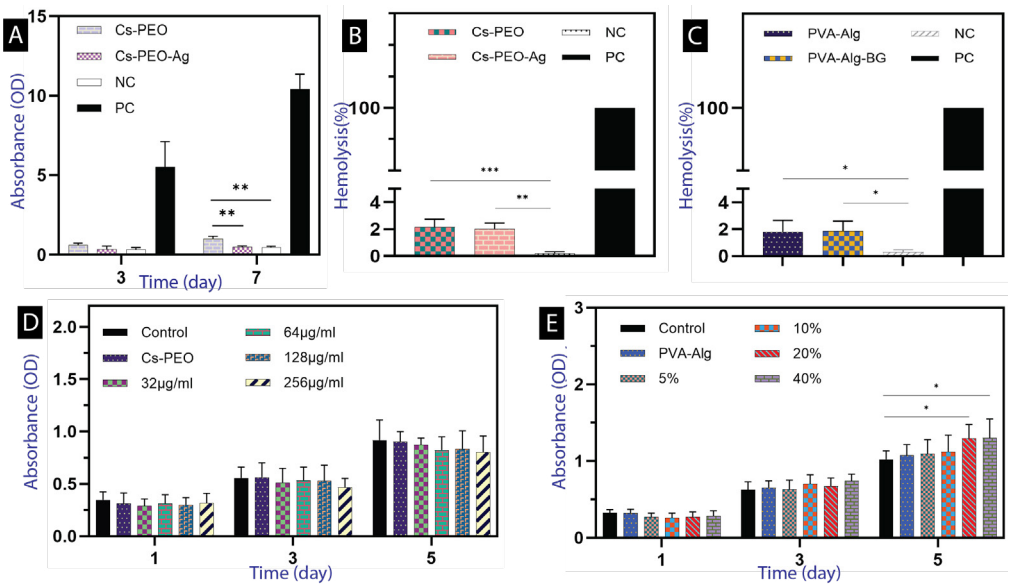

Figure 5. Biological evaluation of scaffolds
Microbial penetration assay showing effective bacterial barrier function of Cs-PEO-AgNPs scaffolds (A); hemocompatibility analysis confirming low hemolysis (<5%) for both electrospun scaffolds (B) and lyophilized hydrogels (C); MTT assay results indicating excellent cytocompatibility of AgNPs-loaded scaffolds (D) and enhanced fibroblast viability with BG-containing hydrogels (E)
Cs-PEO: Chitosan polyethylene oxide; AgNPs: Silver nanoparticles

pore size and moderated swelling behavior—features desirable for controlled exudate management in wound dressings. Comparable contact angle values were found by surface wettability analysis for the Alg-PVA (71.50±8.01°) and Alg-PVA-BG (74.32±6.85°) hydrogels (Figure 4C). Following a 24-hour immersion period, the swelling ratios for Alg-PVA and Alg-PVA-BG were 189.0±12.33% and 147.5±11.42%, respectively (Figure 4D). Alg-PVA and Alg-PVA-BG showed porosity values of 67.30±4.06% and 57.99±2.95%, respectively. Degradation percentages for the Alg-PVA hydrogel were 15.22±2.05% on day 1, 58.91±6.02% on day 3, and 76.22±5.09% on day 5. With weight losses of 13.12±2.33% at day 1, 51.85±7.22% at day 3, and 66.44±5.46% at day 5, the Alg-PVA-BG hydrogel showed lower degradation rates in contrast (Figure 4E). The control container's WVTR was 16,805±4,868 g/m²/day, while the Alg-PVA and Alg-PVA-BG hydrogels had WVTR values of 1,227±119.5 and 1,250±237.1 g/m²/day, respectively. According to biodegradation investigations, both hydrogel formulations showed a quick initial weight loss followed by a plateau phase, indicating controlled degradation behavior.

Biological tests

AgNPs demonstrated robust antibacterial activity, as shown in Table 2.

After three and seven days of exposure, microbial penetration tests showed that both the Cs-PEO and Cs-PEO-AgNPs scaffolds effectively inhibited bacterial penetration. Interestingly, the Cs-PEO-AgNPs group showed negligible microbiological penetration by day 7, which was similar to the negative control (Figure 5A). Results from electrospun scaffolds and lyophilized hydrogels revealed that the hemolysis rate remained about 2%, so they fell within the acceptable range (Figure 5B and 5C)(34, 35). The MTT assay results, performed using L929 murine fibroblasts as a standard model for cytotoxicity screening, showed that while there was no cytotoxicity in the AgNPs-containing electrospun scaffolds (Figure 5D), the hydrogels with 20% and 40% BG exhibited the highest cell viability (Figure 5E). It should be noted that the Day 1 OD values across all groups were relatively low (<0.5), which is attributed to the seeding density of 10,000 cells per well and the initial cell attachment phase, during which metabolic activity is not yet fully up-regulated. However, a clear time-dependent increase in OD values was observed from Day 1 to Day 5 across all groups, confirming progressive cell proliferation and metabolic activity on the scaffolds.

According to the data presented in Figure 6, the migration assay, conducted using HaCaT human keratinocytes to better simulate the re-epithelialization process in a physiologically relevant model, revealed that the Cs-PEO-AgNPs/Alg-PVA-BG group exhibited the highest cell migration rate (42.64±5.84 %) with a statistically significant increase ($p<0.05$) compared to Control and Cs-PEO-Ag-PVA-Alg groups (39.12±2.55 and 39.06±3.82). These findings align with previous studies highlighting the beneficial effects of BG on cell migration due to the presence and release of bioactive ions (36).

Discussion

Green synthesis of AgNPs using plant proteolytic

Table 2. Antimicrobial activity of Bro-AgNPs

Organisms	ATCC	Bro-AgNPs	
		MIC_{90} (μg/ml)	MMC (μg/ml)
Staphylococcus aureus	52268	4	8
Escherichia coli	25922	4	16
Pseudomonas aeruginosa	27853	32	64
Enterococcus faecalis	11700	32	32

Bro-AgNPs: Bromelain- Ag nanoparticles; ATCC: American type culture collection; MMC: Minimum microbicidal concentration

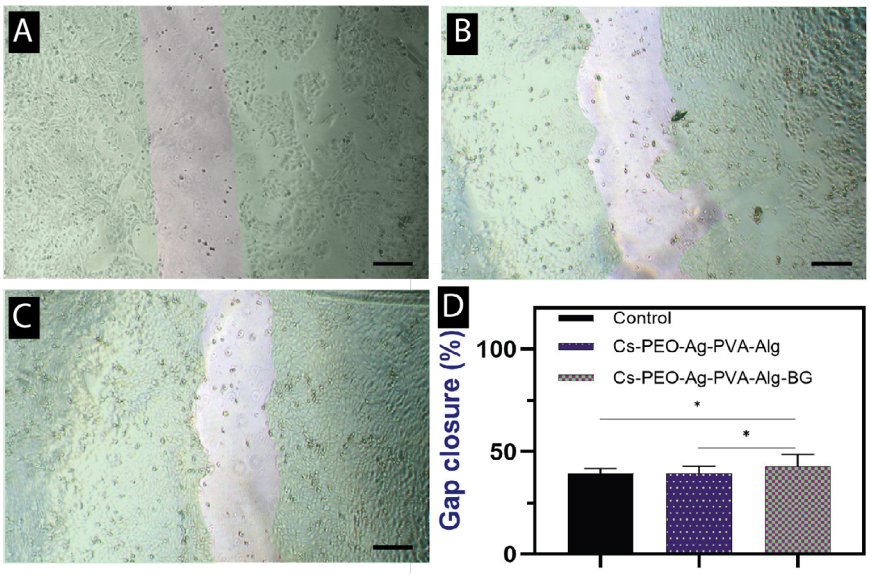

Figure 6. *In vitro* wound closure assay
HaCaT cell migration after 48 h exposure to scaffold extracts: initial scratch wound (A); representative images for control media (B), Cs-PEO-Ag/PVA-Alg (C), and Cs-PEO-Ag/PVA-Alg-BG (D); quantitative analysis showing significantly enhanced migration with bioactive glass (BG) containing composite ($p<0.05$). Scale bar: 500 µm
Cs-PEO: Chitosan polyethylene oxide; AgNPs: Silver nanoparticles

enzymes yielded spherical particles with an average size of 293.22±2.27 nm, consistent with techniques where biological components act as stabilizing and reducing agents (31). DLS analysis confirmed a homogeneous population (200-300 nm), aligning with findings by Khatoon *et al.* (2017) using chemical reduction methods (11). This suggests that AgNP synthesis in this dimension range is replicable across various stabilizing systems. Incorporating AgNPs into the Cs-PEO matrix significantly reduced fiber diameter from 0.76±0.03 µm to 0.40±0.02 µm. This phenomenon is attributed to increased electrostatic interactions between positively charged Cs chains and silver nanoparticles, which strengthen stretching forces on the electrospinning jet (37). The enhanced electrical conductivity of Ag^+ ions further amplifies this effect, producing finer fibers with higher surface area-to-volume ratios, beneficial for cell attachment and nutrient diffusion (34). Both scaffolds exhibited hydrophilic surfaces (contact angle <90°), essential for cellular adhesion, largely due to Cs's amine and carboxyl groups (11). Physicochemical characterization revealed that AgNP incorporation slightly reduced swelling ratios (228.4% vs. 245.7%) due to increased cross-linking density, while maintaining porosity >68% and WVTR within the optimal range (1200–2000 g/m²/day) for wound dressings (38). This balance ensures proper moisture retention without extreme dehydration (39). The progressive biodegradation profile (71.69% weight loss by day 21) synchronizes well with tissue regeneration timelines.

Biological evaluations confirmed the safety and efficacy of the constructs. AgNPs demonstrated concentration-dependent cytocompatibility, with high fibroblast viability at 32 µg/ml but cytotoxicity at higher concentrations (128-256 µg/ml), highlighting the importance of dosage optimization. The antimicrobial performance stems from the synergistic interaction between protonated amine groups of Cs and negatively charged bacterial membranes, reinforced by the broad-spectrum activity of AgNPs (40). Low MIC90 values against S. aureus and *E. coli*, combined with hemolysis levels below 5%, confirm suitability for blood-contacting applications (35).

BG particles exhibited substantial *in vitro* bioactivity, evidenced by HA layer formation upon PBS immersion (41). FTIR and XRD analyses confirmed the preservation of the BG network and crystalline phases (cristobalite and buchwaldite), essential for biological functionality (42). Incorporating BG into Alg-PVA hydrogels reduced pore size (16.81 µm to 14.03 µm) and swelling ratios (189.0% to 147.5%), indicating reinforced network structure through ionic interactions between Ca^{2+} and alginate carboxylates (43). Despite reduced porosity, values remained within the ideal range for cell infiltration (38). BG incorporation also modulated degradation behavior, potentially extending the hydrogel's functional lifespan (24). MTT assays identified 20% BG as the optimal concentration, balancing cell viability and structural stability. The enhanced cellular response is likely driven by regulated release of bioactive ions (e.g., Ca^{2+}), which control signaling pathways linked to migration and proliferation (44). The significantly enhanced fibroblast migration supports this observed in BG-containing composites.

To further elaborate on the biological performance, the distinct use of L929 murine fibroblasts for the MTT assay and HaCaT human keratinocytes for the migration assay warrants discussion. L929 cells are a well-established and reproducible model for initial cytotoxicity screening, providing a reliable baseline for assessing mitochondrial activity and general biocompatibility of biomaterials. In contrast, HaCaT keratinocytes are physiologically more relevant for studying re-epithelialization, as these cells are the primary drivers of wound closure in the epidermal layer. The observed enhancement in HaCaT migration in response to BG-containing scaffolds is particularly significant, as it suggests that the released bioactive ions not only support cell survival but also actively stimulate the migratory machinery essential for wound healing. This finding aligns with previous reports indicating that ionic dissolution products

are crucial for cell detachment and movement (12). Also, the relatively low baseline OD values observed at Day 1 in the MTT assay (<0.5) are attributed to the intentionally low seeding density of 10,000 cells per well and the initial cell attachment phase, during which mitochondrial metabolic activity may not yet be fully up-regulated. At this early time point, cells are primarily adapting to the scaffold surfaces rather than actively proliferating. This is consistent with previous reports indicating that cells require 24-48 hours to establish adhesion and enter the logarithmic growth phase, after which metabolic activity and OD values increase substantially. Importantly, the progressive increase in OD values from Day 1 to Day 5 across all groups confirms that cells remained metabolically active and viable on the scaffolds; viability percentages were calculated relative to the control group at each respective time point, ensuring an accurate and reliable assessment of cytocompatibility (18).

Mechanistically, AgNPs aid healing by releasing Ag^+ ions that disrupt bacterial membranes and modulate inflammatory cytokines (45), while BG activates signaling pathways implicated in ECM remodeling via ionic dissolution (46). The combination of these two functionalities within a bilayer construct addresses two major challenges in wound healing simultaneously: preventing bacterial infection and promoting tissue regeneration. The upper AgNP-loaded Cs-PEO layer acts as a protective antimicrobial barrier, reducing the risk of wound contamination. At the same time, the lower BG-enriched Alg-PVA hydrogel provides a bioactive niche that supports cell infiltration, proliferation, and migration. This spatial separation of functions is a key advantage of our bilayer design, as it allows each layer to be optimized independently for its specific role without compromising the other's performance.

Compared with previous studies, the swelling ratio and porosity values obtained in this work are comparable to or better than those reported for other alginate-based wound dressings (47, 48). The controlled degradation rate of our hydrogel (71.69% over 21 days) is particularly advantageous, as it closely matches the natural wound healing timeline, ensuring that the scaffold provides mechanical support during the early proliferative phase while gradually degrading to make room for newly formed tissue. This contrasts with some previously reported systems that either degrade too rapidly, losing structural integrity before adequate tissue formation, or too slowly, hindering tissue remodeling (49, 50).

Despite the promising *in vitro* results, we acknowledge that the findings of this study are primarily based on cell culture models and may not fully replicate the complex *in vivo* wound healing environment, which involves multiple cell types, immune responses, angiogenesis, and dynamic biochemical signals. Nevertheless, the robust antibacterial activity, excellent cytocompatibility, and enhanced cell migration observed *in vitro* strongly support the translational potential of this bilayer scaffold. Future studies will focus on evaluating the scaffold in full-thickness excisional wound models in rodents to assess its efficacy, degradation profile, and host tissue integration in a physiologically relevant setting.

Conclusion

In conclusion, this study validates the physicochemical and *in vitro* biological efficacy of a bilayer wound dressing strategy. The nanofibrous top layer provides essential infection control, while the bioactive hydrogel matrix facilitates tissue integration through ECM mimicry and ion release. The synergistic design balances antimicrobial protection with regenerative capacity, positioning this scaffold as a promising candidate for future clinical translation in full-thickness wound management.

Acknowledgment

The results described in this paper were part of the student thesis of Elham Rahmanian, which was financially supported by Shiraz University of Medical Sciences, Shiraz, Iran (Grant No 28940), and approved under ethics number IR.SUMS.AEC.1403.076.

Authors' Contributions

E R assisted with writing the original draft and methodology; H B, N T, Z Z, AM A, and S K contributed to methodology; A V provided supervision, contributed to methodology, and helped with original draft writing, reviewing, and editing; F D supervised, curated data, handled conceptualization, and participated in reviewing and editing.

Conflicts of Interest

The authors declare that they have no competing interests.

Declaration

We acknowledge the use of DeepSeek for language editing and minor text refinement. The authors take full responsibility for the content of the manuscript.

References

1. Murray CJ, Barber RM, Foreman KJ, Ozgoren AA, Abd-Allah F, Abera SF, *et al.* Global, regional, and national disability-adjusted life years (DALYs) for 306 diseases and injuries and healthy life expectancy (HALE) for 188 countries, 1990-2013: Quantifying the epidemiological transition. Lancet 2015; 386: 2145-2191.
2.Yu R, Zhang H, Guo B. Conductive biomaterials as bioactive wound dressing for wound healing and skin tissue engineering. Nanomicro Lett 2021; 14: 1.
3. Almuhayawi M. Efficacy of Nigella sativa in Wound Healing. Indian J Pharm Sci 2023; 85: 173-181.
4. Narimanpour Z, Nazm Bojnordi M, Somayeh E-B, Elham V, Jamileh S, Ghasemi H. Silk nanofibrous electrospun scaffold amplifies proliferation and stemness profile of mouse spermatogonial stem cells. Regen Eng Transl Med 2022; 8: 86-93.
5. Salehi M, Vaez A, Naseri-Nosar M, Farzamfar S, Ai A, Ai J, *et al.* Naringin-loaded poly (ε-caprolactone)/gelatin electrospun mat as a potential wound dressing: *In vitro* and *in vivo* evaluation. Fibers Polymers 2018; 19: 125-134.
6. Emamgholi A, Sadri M, Sadraee SH, Hosseini SH. The synthesis of chitosan/polyethylene nanofibersoxide on chitosan membrane: An applicable model in tissue engineering. Ann Milit Health Sci Res 2013; 10: 300-305.
7. Bagheri M, Validi M, Gholipour A, Makvandi P, Sharifi E. Chitosan nanofiber biocomposites for potential wound healing applications: Antioxidant activity with synergic antibacterial effect. Bioeng Transl Med 2022; 7: e10254.
8. Kharat Z, Goushki MA, Sarvian N, Asad S, Dehghan MM, Kabiri M. Chitosan/PEO nanofibers containing *Calendula officinalis* extract: Preparation, characterization, *in vitro* and *in vivo* evaluation for wound healing applications. Int J Pharm 2021; 609: 121132.
9. Naeimi M, Tajedin R, Farahmandfar F, Naeimi M, Monajjemi M. Preparation and characterization of vancomycin-loaded chitosan/

PVA/PEG hydrogels for wound dressing. Mat Res Exp 2020; 7: 095401.
10. Tahamtan MS, Ansari F, Kasmaie FM, Zareshahrabadi Z, Amani AM, Salehi M, *et al.* Integration of green synthesized silver nanoparticles in electrospun PVA-alginate and resveratrol-loaded ZIF-8 into alginate lyophilized hydrogel as a dual-layered biomimetic skin construct. Int J Biol Macromol 2025; 338: 149681.
11. Khatoon UT, Rao GN, Mohan KM, Ramanaviciene A, Ramanavicius A. Antibacterial and antifungal activity of silver nanospheres synthesized by tri-sodium citrate assisted chemical approach. Vacuum 2017; 146: 259–265.
12. Najafian-Najafabadi A, Salehi M, Amani AM, Ebrahiminezhad A, Vojoudi E, Dortaj H, *et al.* Biomimetic skin regeneration using a dual-layer scaffold/hydrogel: Polycaprolactone-gelatin electrospun scaffold incorporated with bromelain-silver nanoparticles and alginate hydrogel enriched with selenium-doped bioglass. Int J Biol Macromol 2025; 311: 143733.
13. AshaRani P, Low Kah Mun G, Hande MP, Valiyaveettil S. Cytotoxicity and genotoxicity of silver nanoparticles in human cells. ACS Nano 2009; 3: 279-290.
14. Wathoni N, Herginto AS, Suhandi C, Elamin KM, Mohammed AFA, Mahmoud SA, *et al.* Advancements in alginate- based biomaterials for enhanced skin regeneration: A comprehensive review. Int J Polym Sci 2026; 2026: 8996702.
15. Jiao T, Lian Q, Lian W, Wang Y, Li D, Reis RL, *et al.* Properties of collagen/sodium alginate hydrogels for bioprinting of skin models. J Bionic Eng 2023; 20: 105–118.
16. Knill C, Kennedy J, Mistry J, Miraftab M, Smart G, Groocock M, *et al.* Alginate fibres modified with unhydrolysed and hydrolysed chitosans for wound dressings. Carbohydr Polymers 2004; 55: 65-76.
17. Rhim J-W. Physical and mechanical properties of water resistant sodium alginate films. LWT-Food Sci Technol 2004; 37: 323-330.
18. Mahjoub G, Zareshahrabadi Z, Vaez A, Rasaee MJ. Engineered dual-layered polyvinyl alcohol-alginate wound dressings incorporating antimicrobial and pro-healing functions. Int J Biol Macromol 2026; 345: 150369.
19. Kozma M, Acharya B, Bissessur R. Chitin, chitosan, and nanochitin: Extraction, synthesis, and applications. Polymers 2022; 14: 3989.
20. Massera J. Bioactive glass in tissue engineering: Progress and challenges. Adv Tissue Eng Regen Med 2016; 1: 1-2.
21. Mehrabi T, Mesgar AS, Mohammadi Z. Bioactive glasses: A promising therapeutic ion release strategy for enhancing wound healing. ACS Biomater Sci Eng 2020; 6: 5399-5430.
22. Zhu Y, Zhang X, Chang G, Deng S, Chan HF. Bioactive glass in tissue regeneration: Unveiling recent advances in regenerative strategies and applications. Adv Mater 2025; 37: 2312964.
23. Gabbai-Armelin PR, Wilian Kido H, Fernandes KR, Fortulan CA, Muniz Renno AC. Effects of bio-inspired bioglass/collagen/magnesium composites on bone repair. J Biomater Appl 2019; 34: 261-272.
24. Wu R, Huang L, Xia Q, Liu Z, Huang Y, Jiang Y, *et al.* Injectable mesoporous bioactive glass/sodium alginate hydrogel loaded with melatonin for intervertebral disc regeneration. Mater Today Bio 2023; 22: 100731.
25. Shehabeldine A, El-Hamshary H, Hasanin M, El-Faham A, Al-Sahly M. Enhancing the antifungal activity of griseofulvin by incorporation a green biopolymer-based nanocomposite. Polymers 2021; 13: 542.
26. Ziai Y, Lanzi M, Rinoldi C, Zargarian SS, Zakrzewska A, Kosik-Kozioł A, *et al.* Developing strategies to optimize the anchorage between electrospun nanofibers and hydrogels for multi-layered plasmonic biomaterials. Nanoscale Adv 2024; 6: 1246–1258.
27. Bagher Z, Ehterami A, Safdel MH, Khastar H, Semiari H, Asefnejad A, *et al.* Wound healing with alginate/chitosan hydrogel containing hesperidin in rat model. J Drug Deliv Sci Technol 2020; 55: 101379.
28. Astm E. Standard test methods for water vapor transmission of materials. ASTM International: West, Conshohocken, PA; 96.
29. Rodríguez-Melcón C, Alonso-Calleja C, García-Fernández C, Carballo J, Capita R. Minimum inhibitory concentration (MIC) and minimum bactericidal concentration (MBC) for twelve antimicrobials (biocides and antibiotics) in eight strains of *Listeria monocytogenes*. Biology 2021; 11: 46.
30. Shahriari-Khalaji M, Sattar M, Cao R, Zhu M. Angiogenesis, hemocompatibility and bactericidal effect of bioactive natural polymer- based bilayer adhesive skin substitute for infected burned wound healing. Bioactive Mater 2023; 29: 177-195.
31. Najafian-Najafabadi A, Salehi M, Amani AM, Ebrahiminezhad A, Vojoudi E, Dortaj H, *et al.* Biomimetic skin regeneration using a dual-layer scaffold/hydrogel: Polycaprolactone-gelatin electrospun scaffold incorporated with bromelain-silver nanoparticles and alginate hydrogel enriched with selenium-doped bioglass. Int J Biol Macromol 2025; 311: 143733.
32. Parimi MR, Gantala DD, Deepala NA, Bikkina SSY, Reddy JMK, Vangalapati M. Optimization of Bromelain extraction from green papaya (Carica papaya) peel waste and its application in the recovery of silver from waste of X-ray photographic films. Environ Sci Pollut Res 2024; 7: 1–17.
33. Saghafi Y, Baharifar H, Najmoddin N, Asefnejad A, Maleki H, Sajjadi-Jazi SM, *et al.* Bromelain-and silver nanoparticle-loaded polycaprolactone/chitosan nanofibrous dressings for skin wound healing. Gels 2023; 9: 672.
34. McNamee AP, Simmonds MJ. Red blood cell sublethal damage: Hemocompatibility is not the absence of hemolysis. Transfus Med Rev 2023; 37: 150723.
35. de la Harpe KM, Kondiah PP, Choonara YE, Marimuthu T, du Toit LC, Pillay V. The hemocompatibility of nanoparticles: a review of cell–nanoparticle interactions and hemostasis. Cells 2019; 8: 1209.
36. Tsai F-C, Kuo G-H, Chang S-W, Tsai P-J. Ca2+ signaling in cytoskeletal reorganization, cell migration, and cancer metastasis. BioMed Res Int 2015; 2015: 409245.
37. Sarker B, Li W, Zheng K, Detsch R, Boccaccini AR. Designing porous bone tissue engineering scaffolds with enhanced mechanical properties from composite hydrogels composed of modified alginate, gelatin, and bioactive glass. ACS Biomater Sci Eng 2016; 2: 2240-2254.
38. O'brien FJ. Biomaterials & scaffolds for tissue engineering. Mater Today 2011; 14: 88-95.
39. Mouseli S, Natouri O, Seghinsara AM, Ghorbani M, Mokhtarzadeh AA, Moghadam FM. Physicochemical and biological characterization of propolis-loaded composite polyamide-6/soybean protein nanofibers for wound healing applications. Colloids Surf A Physicochem Eng Asp 2024; 694: 134172.
40. Kumar-Krishnan S, Prokhorov E, Hernández-Iturriaga M, Mota-Morales JD, Vázquez-Lepe M, Kovalenko Y, *et al.* Chitosan/silver nanocomposites: Synergistic antibacterial action of silver nanoparticles and silver ions. Eur Polym J 2015; 67: 242-251.
41. Fathi M, Mohammadi AD. Preparation and characterization of sol–gel bioactive glass coating for improvement of biocompatibility of human body implant. Mater Sci Eng A 2008; 474: 128-133.
42. Mishra RK, Pradhan BL, Parveen S, Behera P, Avinashi SK, Kumari S, *et al.* Fabrication of bioactive transparent glass ceramics 55SiO2–25Na2O-(15-x) CaO–5P2O5-xZrO2 (0≤ x≤ 6): Physical, structural and *in vitro* cell viability insights for biomedical applications. Ceramics Int 2024; 50: 14550–14570.
43. Wu J, Lin J, Zhou M, Wei C. Synthesis and properties of starch-graft- polyacrylamide/clay superabsorbent composite. Macromol Rapid Commun 2000; 21: 1032-1034.
44. Khademi S, Shokrolahi P, Irani S. Gelatin-chitosan coating enhances L929 fibroblasts proliferation on supramolecular nano-fibrous scaffolds. Cell Mol Res 2016; 28: 500–512.
45. Chen X, Ran X, Wei X, Zhu L, Chen S, Liao Z, *et al.* Bioactive glass 1393 promotes angiogenesis and accelerates wound healing through ROS/P53/MMP9 signaling pathway. Regen Ther 2024; 26: 132–144.

46. Balaure PC, Adelina-Gabriela N, Anghel D, Grumezescu AM, Adina A. Role of silver nanoparticles in wound healing: Mechanisms, efficacy, and clinical applications. Inorganics 2025; 13: 401.
47. Malektaj H, Drozdov AD, deClaville Christiansen J. Swelling of homogeneous alginate gels with multi-stimuli sensitivity. Int J Mol Sci 2023; 24.
48. Salarizadeh N, Salimi Sabour E, Hushmandi K. Two-layered sodium alginate/polyvinyl alcohol/chitosan-based nanocomposite wound dressing with Hyssopus officinalis extract for enhanced wound healing. Ind Crops Prod 2025; 235: 121736.
49. Barceló X, Eichholz KF, Garcia O, Kelly DJ. Tuning the degradation rate of alginate-based bioinks for bioprinting functional cartilage tissue. Biomedicines 2022; 10: 1621.
50. Hou H, Lanzi AM, Feng Y, Raavi, Vegas AJ. Alginate hydrogels with tunable degradation. Macromol Rapid Commun 2026; 47: e00348.